NANO LETTERS

Letter

pubs.acs.org/NanoLett

Synthesis of MoS_2 and $MoSe_2$ Films with Vertically Aligned Layers

Desheng Kong,[†] Haotian Wang,[‡] Judy J. Cha,[†] Mauro Pasta,[†] Kristie J. Koski,[†] Jie Yao,[†] and Yi Cui*[,†,§]

[†]Department of Materials Science and Engineering, Stanford University, Stanford, California 94305, United States

[‡]Department of Applied Physics, Stanford University, Stanford, California 94305, United States

[§]Stanford Institute for Materials and Energy Sciences, SLAC National Accelerator Laboratory, 2575 Sand Hill Road, Menlo Park, California 94025, United States

Supporting Information

ABSTRACT: Layered materials consist of molecular layers stacked together by weak interlayer interactions. They often crystallize to form atomically smooth thin films, nanotubes, and platelet or fullerene-like nanoparticles due to the anisotropic bonding. Structures that predominately expose edges of the layers exhibit high surface energy and are often considered unstable. In this communication, we present a synthesis process to grow MoS_2 and $MoSe_2$ thin films with vertically aligned layers, thereby maximally exposing the edges on the film surface. Such edge-terminated films are metastable structures of MoS_2 and $MoSe_2$, which may find applications in diverse catalytic reactions. We have confirmed their catalytic activity in a hydrogen evolution reaction (HER), in which the exchange current density correlates directly with the density of the exposed edge sites.

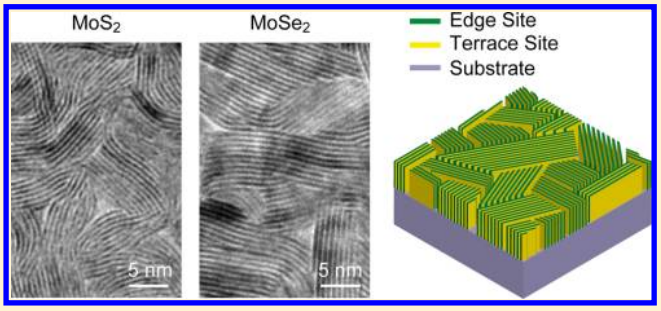

KEYWORDS: *Layered materials, MoS_2, $MoSe_2$, hydrogen evolution reaction, sulfurization, selenization*

Layered materials consist of planar, two-dimensional molecular layers stacked together by weak interlayer interactions. Each layer is formed by strong chemical bonding. The highly anisotropic structure allows top-down exfoliation to obtain ultrathin flakes by mechanical or chemical processes,[1−11] and bottom-up synthesis of thin films, nanoplates, nanoribbons, inorganic nanotubes, and fullerene-like nanoparticles.[12−26] In reduced dimensions, it is scientifically intriguing to study nanostructures of layered material as their electronic structures are often distinctive from their bulk counterpart.[3,27−29] Layered materials usually expose the basal planes as the terminating surface with minimal roughness and dangling bonds, which are ideal for electronic device applications.[30−32] Another form of layered materials is the three-dimensional closed nanotube and fullerene-like nanoparticle, which is attractive as a solid lubricant and electronic material.[26,33] In contrast, less effort has been made to use the edges of these layered materials. The edges are full of dangling bonds and chemically active to manipulate the properties of the layered materials, for example in n-type doping for graphene.[34] In addition, the edges of layered materials are also the active sites for many important catalytic reactions, such as hydrodesulfurization,[35,36] hydrogen evolution reaction (HER),[37,38] oxygen reduction reactions,[39] and methane conversion.[40] However, edges are usually the rare surface sites of layered materials due to their inherently high surface energy. Increasing the edge dimension is therefore challenging.[41] Here, we develop a rapid sulfurization/selenization process to convert Mo thin films into polycrystalline molybdenum dichalcogenide films, including molybdenum disulfide (MoS_2) and molybdenum diselenide ($MoSe_2$), in which the molecular layers are aligned vertically to maximally expose the edges. We find that these films are stable HER catalysts with large exchange current densities. $MoSe_2$, introduced here as a novel HER catalyst, exhibits comparable catalytic activity to MoS_2.

MoS_2 and $MoSe_2$ share similar crystal structures where the two-dimensional molecular layers are linked by van der Waals interaction, as shown in Figure 1a. Each charge-neutral layer consists of three covalently bonded atomic sheets, for example S−Mo−S in MoS_2, with a layer-to-layer distance of about 6 Å. Two general types of surface sites are present on these crystals: terrace sites on the basal planes and edge sites on the side surfaces. Due to the anisotropic bonding and the general tendency to minimize the surface energy, nanoparticles of layer materials usually exhibit platelet-like morphology, in which the basal planes are exposed, as shown schematically in Figure 1b (left).[7,22,38,42] Alternatively, fullerene-like nanoparticles and inorganic nanotubes can also form by folding the layers, as illustrated in Figure 1b (right). Such completely closed structures have been also obtained in experiments and well-explained with the surface energy arguments.[24−26,33,43] A conceptually distinctive structure would be one in which the entire surface area is covered with the edges. It can be achieved by vertically aligning the layers with respect to the film, as illustrated in Figure 1c, thereby maximally exposing the edge

Received: January 21, 2013

   dx.doi.org/10.1021/nl400258t | *Nano Lett.* XXXX, XXX, XXX−XXX

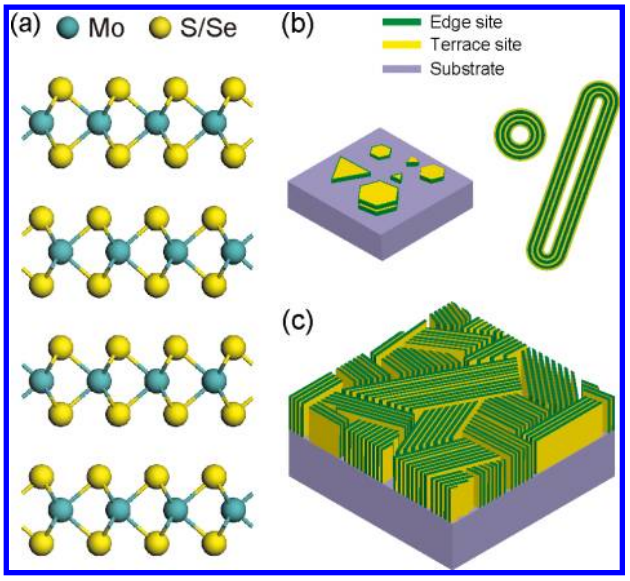

Figure 1. Nanostructures of layered MoS_2 and $MoSe_2$. (a) Layered crystal structure of molybdenum chalcogenide with individual S−Mo−S (or Se−Mo−Se) layers stacked along the *c*-axis by weak van der Waals interaction. The highly anisotropic crystal structure is the origin of anisotropic electrical and chemical properties. (b) Schematics of MoS_2 nanoparticle with platelet-like morphology distributed on a substrate (left), and nanotubes and fullerene-like nanotubes of MoS_2 and $MoSe_2$ (right). (c) Idealized structure of edge-terminated molybdenum chalcogenide films with the layers aligned perpendicular to the substrate, maximally exposing the edges of the layers.

sites. As a metastable structure, such an edge-terminated film has been often considered unstable. In the case of MoS_2 and $MoSe_2$, the surface energy of the edge sites is larger than that of the terrace sites by 2 orders of magnitude.[44] Here, we demonstrate that the edge-terminated structure can be synthesized on diverse substrates through a kinetically controlled rapid growth method.

The molybdenum chalcogenide films are converted from e-beam evaporated, ultrathin Mo films (~5 nm thick) by a rapid sulfurization/selenization process in a horizontal tube furnace, where elemental sulfur/selenium powders are used as the precursors. The synthesis setup schematic is illustrated in Figure 2a. This process yields smooth and uniform films as shown in Figure 2b, which is further confirmed by atomic force microscopy (AFM) measurements (Supporting Information Table S9). We employ transmission electron microscopy (TEM) tomography to reconstruct the three-dimensional (3D) structure of a representative MoS_2 film. Developments in electron tomography allow the three-dimensional visualization and analysis of materials at nanometer scale along arbitrary viewing directions.[45−48] Here, aberration-corrected TEM images were acquired for the tomography tilt series to achieve the highest resolution possible in the reconstructed data set (Supporting Information, Figure S1). Every tilt image clearly shows the contrast fringes of individual layers. In Figure 2c, the tomogram reveals domains of striped patterns where the stripes span from the top surface to the bottom surface of the film (Supporting Information Movies S11 and S12 display the cross sections of the reconstructed MoS_2 film sequentially to show the resolved layers throughout the film thickness at different viewing angles). The spacing between the stripes is ~6.3 Å, which is consistent with the interlayer spacing of MoS_2. Thus, we confirm that the whole film is terminated by MoS_2 edges. A statistical analysis of the tilt angles of the vertical layers in different domains, obtained from the cross sections of the reconstructed data, shows that the MoS_2 layers are predom-

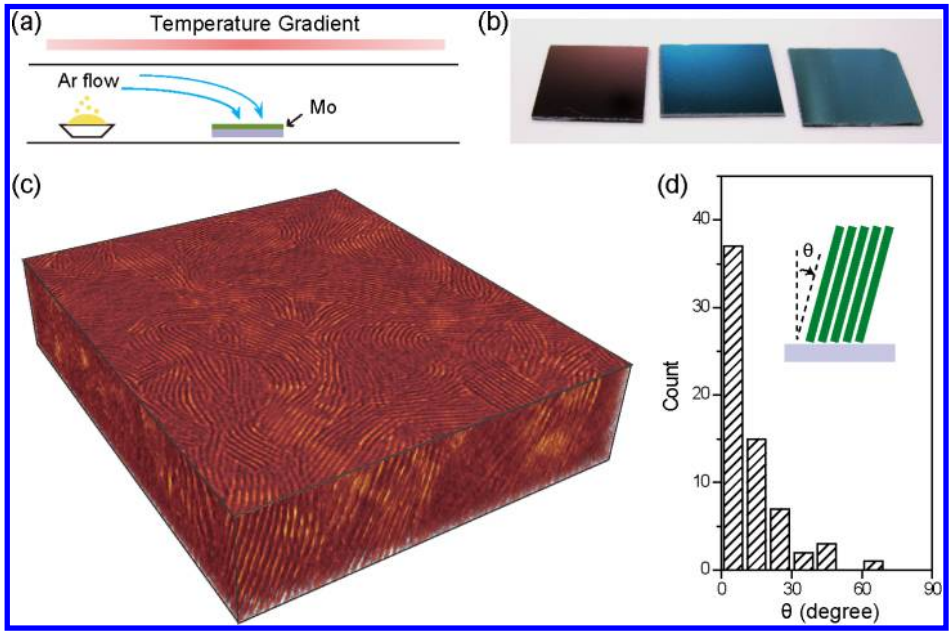

Figure 2. Synthesis setup and as-grown films. (a) Schematic of the synthesis setup in a horizontal tube furnace. (b) Digital photos of a pristine oxidized silicon (300 nm SiO_2/Si) substrate (left), a MoS_2 film on oxidized silicon (middle), and a $MoSe_2$ film on oxidized silicon (right). Each substrate is about 1.5 × 1.5 cm^2 in dimension. (c) Volume-rendered reconstructed TEM tomogram of a MoS_2 film grown by rapid sulfurization, which resembles the ideal edge-terminated structure. Individual layers are clearly resolved in this volume-rendered image, with the interlayer spacing of about 6.3 Å. Movies S1 and S2 display the cross sections of the reconstructed MoS_2 film moving throughout the film thickness. (d) Statistical distribution of tilt angles (θ) of layers in individual grains in edge-terminated MoS_2 film, where the tilt angle is defined in the inset. The statistics include all grains in the reconstructed tomogram.

dx.doi.org/10.1021/nl400258t | *Nano Lett.* XXXX, XXX, XXX−XXX

inantly aligned perpendicular to the film (Figure 2d, Supporting Information Figure S2). The film therefore resembles the proposed structure in Figure 1c which maximally exposes the edge sites on the surface.

Further structural characterizations provide additional insights into these films. Figure 3a shows a typical TEM image of

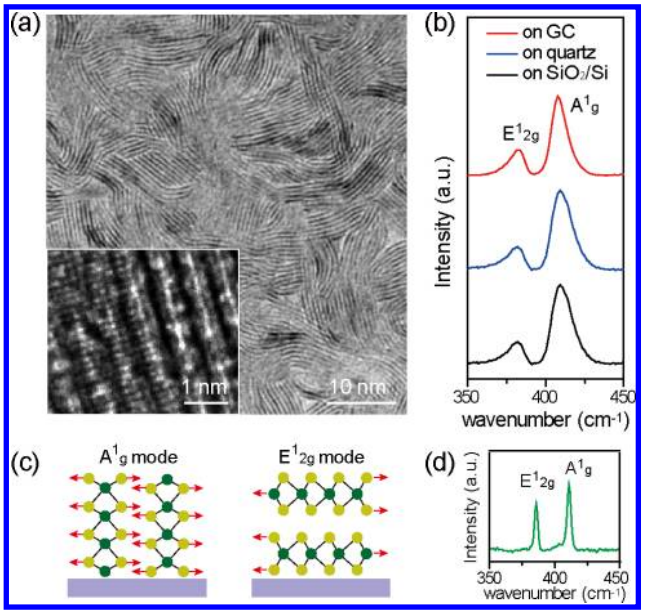

Figure 3. (a) TEM image of a MoS_2 film produced by rapid sulfurization, clearly showing exposed edges. High-resolution TEM image (inset) reveals individual layers consisting of three atomic planes in the sequence of S−Mo−S. (b) Raman spectra from MoS_2 films grown on glassy carbon (GC), quartz, and oxidized silicon (300 nm SiO_2/Si) substrates, respectively. (c) Schematics of preferentially excited A^1_g Raman mode for edge-terminated film (top), and E^1_{2g} mode for terrace-terminated film (bottom). (d) Raman spectrum from a terrace-terminated surface of a MoS_2 single crystal.

MoS_2 film with densely packed, stripe-like grains. Each grain is about 10 nm long and several nanometers wide. In the inset of Figure 3a, the high-resolution TEM image on a single grain reveals individual atomic planes ordered in the S−Mo−S sequence to form each layer. The unique edge-terminated MoS_2 films can be grown on various substrates using the same growth procedure. Figure 3b presents Raman spectra collected from MoS_2 films grown on glassy carbon (GC), quartz, and oxidized silicon (300 nm SiO_2/Si). All three spectra show consistent spectral features. Notice that the Raman peak corresponding to the out-of plane Mo−S phonon mode (A^1_g) is preferentially excited for edge-terminated film due to the polarization dependence, whereas the in-plane Mo−S phonon mode (E^1_{2g}) is preferentially excited for terrace-terminated film,[49] as illustrated in Figure 3c. Accordingly, the relative integrated intensities between the two Raman modes provide texture information of the film. As a reference, the Raman spectrum from a terrace surface of MoS_2 single crystal is shown in Figure 3d, with the intensity of E^1_{2g} mode close to that of A^1_g mode, in sharp contrast to the spectra of edge-terminated films with a small E^1_{2g} peak about 30% of A^1_g peak. Similarly, TEM and Raman studies on $MoSe_2$ films, shown in Figure 4a and b, confirm nearly vertically aligned layers. The dimensions of individual grains in $MoSe_2$ films are about 20 nm long and several nanometers wide, slightly larger than those in MoS_2 films.

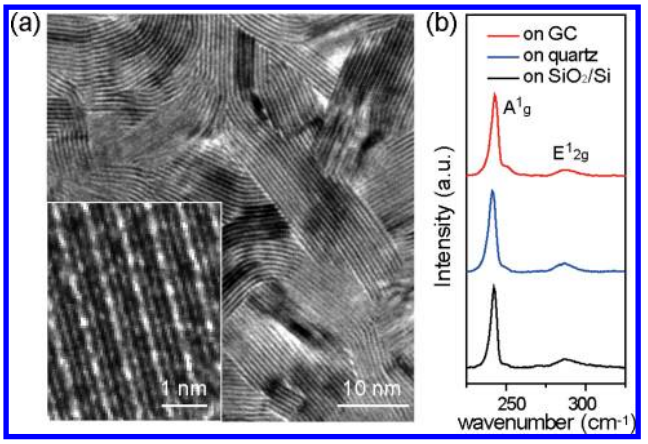

Figure 4. (a) TEM image of a $MoSe_2$ film produced by rapid selenization showing exposed edges. Corresponding high-resolution TEM image (inset) reveals individual layers consisting of Se−Mo−Se atomic planes. (b) Raman spectra from edge-terminated $MoSe_2$ films grown on glassy carbon (GC), quartz, and oxidized silicon (300 nm SiO_2/Si) substrates, respectively.

A sulfurization process was previously used to produce layered chalcogenide such as MoS_2 and WS_2, but predominantly with exposed low-energy terraces.[50] Such process has also been widely employed to produce inorganic nanotubes and fullerene-like nanoparticles.[24,25] The distinction can be partially understood based on previous studies on chalcogenide film synthesis. It was noticed that the sulfurization/selenization conditions largely affect the layer orientations in the film.[51,52] The formation of the vertically aligned layers in our case is likely to be driven by kinetic process as illustrated in Figure 5.

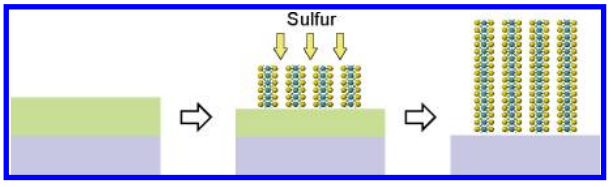

Figure 5. Schematic of the proposed synthesis mechanism. The sulfurization/selenization reaction requires the diffusion of sulfur/selenium into the film and converts it into sulfide/selenide. Mass transport along the layers through van der Waals gaps is much faster than across the layers in MoS_2/$MoSe_2$. Consequently, the layers tend to be perpendicular to the substrate, with exposed van der Waals gaps for fast reaction.

During the sulfurization/selenization, sulfur/selenium vapor diffuses into Mo film and converts it into sulfide/selenide. At high temperature, the chemical conversion occurs much faster than the diffusion of sulfur/selenium gas into the film, thereby making sulfur/selenium diffusion as the rate-limiting process. Due to the anisotropic structure of MoS_2/$MoSe_2$, diffusion along the layers through van der Waals gaps is expected to be much faster than diffusion across the layers. Accordingly, the layers naturally orient perpendicular to the film, exposing van der Waals gaps for fast reaction. Additional experiments are still required to figure out the critical factors that control the layer orientation. We suspect the different sulfurizing precursors, elemental S used here with respect to hydrogen sulfide (H_2S) in other studies,[25,41,50] may account for the difference. Thermal annealing experiments discussed in later section further strengthen the proposed kinetically driven growth process.

dx.doi.org/10.1021/nl400258t | Nano Lett. XXXX, XXX, XXX−XXX

The edge terminated film is an attractive candidate material for catalysis. In particular, the benefits of these films as electrochemical HER catalysts lie in following aspects. The films offer the maximal edge sites over a given specific area, and HER activity is driven by these edge sites.[37,38] In addition, the structure of the film guarantees efficient charge flow from the conductive support to active surface sites along individual layers. It is in fact a general consideration in designing MoS_2 HER catalysts to minimizing ohmic loss,[53,54] as the interlayer conductivity is 2 orders of magnitude lower than intralayer conductivity.[55,56] Here, we evaluate the catalytic activity of edge-terminated MoS_2 and $MoSe_2$ films based on samples grown on mirror-polished glassy carbon substrates. Glassy carbon is the ideal substrate, thanks to its negligible HER activity in the measurement voltage range and chemical stability in corrosive electrolyte. Measurements are performed in a 0.5 M H_2SO_4 solution using a typical three-electrode cell setup (see Methods). Electrochemical impedance spectroscopy (EIS) reveals negligible ohmic resistance of these films (Supporting Information, Figure S5), consistent with the expected efficient intralayer charge transport. Typical cathodic polarization curves and corresponding Tafel plots are shown in Figure 6a and b

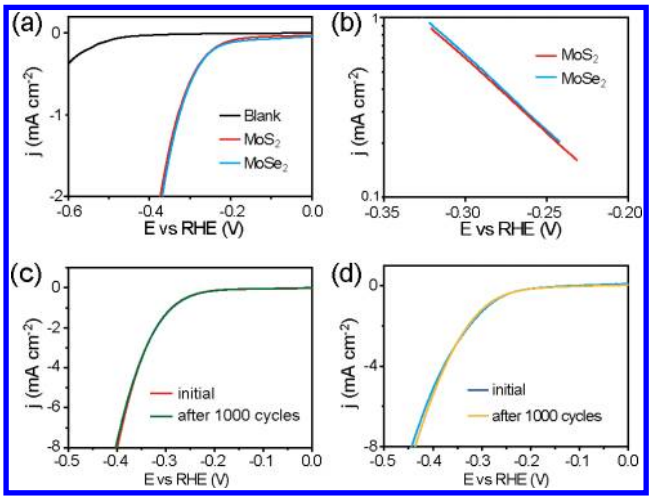

Figure 6. Electrochemical measurements in a cathodic potential window. (a) Polarization curves of edge-terminated MoS_2 and $MoSe_2$ films as well as a blank glassy carbon substrate showing H_2 evolution. (b) Corresponding Tafel plot (log current versus potential). Catalyst stability tests for MoS_2 (c) and $MoSe_2$ (d) in which negligible HER currents are lost after 1000 cycles in the cathodic potentials windows.

respectively. Notice that the current presented here is the surface-area-normalized kinetic current, based on the specific surface area acquired by AFM (Supporting Information, Table S9). The exchange current density, j_0, is determined by fitting the linear portion of Tafel plot at low cathodic current to the Tafel equation,[38,57] yielding averaged values of 2.2×10^{-6} A/cm^2 for MoS_2 and 2.0×10^{-6} A/cm^2 for $MoSe_2$ (Supporting Information, Table S10). The structural characterization based on TEM studies allow us to calculate edge site density and to directly correlate the activity to each edge site, yielding a turn over frequency (TOF) at 0 V of 0.013 s^{-1} for MoS_2 and 0.014 s^{-1} for $MoSe_2$ (Table 1). The TOF of MoS_2 is very close to the reported value of 0.016 s^{-1} obtained from combined STM studies and in situ electrochemical measurements on MoS_2 nanoplatelet catalysts.[38] The close agreement of TOFs between our ex situ measurements on edge-terminated MoS_2 films and

Table 1. TOFs of the Active Edge Site on Edge-Terminated MoS_2 and $MoSe_2$ Films[a]

materials	exchange current density (A/cm^2)	exchange current per site (A/site)	TOF (s^{-1})
MoS_2	2.2×10^{-6}	4.1×10^{-21}	0.013
$MoSe_2$	2.0×10^{-6}	4.5×10^{-21}	0.014

[a]The lattice parameters from reference X-ray diffraction patterns (PDF cards no. 00-037-1492 for MoS_2 and 04-004-8782 for $MoSe_2$) are used to calculate the densities of active sites. We use the interlayer distance instead of the layer spacing on the film to simplify the calculation (Supporting Information, Fig. S2 and discussion therein).

in situ studies on nanoparticulate catalyst is significant. It confirms that nearly all of the surface sites on edge-terminated films are catalytically active. Due to the increased number of edge sites, the exchange current densities of edge-terminated films are about ten times higher than previous MoS_2 nanoparticle-based electrodes[38] and compare favorably to most common metal catalysts.[57] The similar HER activity between $MoSe_2$ and MoS_2 suggests the Mo atoms are likely the main active centers on the edges, as already observed in the hydrodesulfurization reaction.[58] This conclusion is further supported by the general observation of HER activities for MoS_2 edges,[37,38] amorphous MoS_x films,[59] incomplete cubane-type $[Mo_3S_4]^{4+}$ clusters,[60] and Mo^{IV}-disulfide complexes,[61] with slightly varying Mo−S bonding structures.

The Tafel Slopes measured from multiple samples are in the range of 105−120 mV/dec (Supporting Information, Table S10), which suggests that the rate-determining step in the HER mechanism on our MoS_2 and $MoSe_2$ catalyst is the Volmer reaction,[62,63] a discharge step that converts protons into absorbed hydrogen atoms on the catalyst surface. Previous studies on MoS_2 catalyst has shown a large spread of Tafel slopes ranging from 40 mV to 120 mV/dec.[38,41,42,50,59,64] Tafel slopes observed here are on the larger side of this range. A small Tafel slope is desired for practical application of HER catalysts, and the overall perfomance of edge-terminated MoS_2 and $MoSe_2$ films should be further improved. Our preliminary study suggests the slow discharge reaction can be partially accelerated by tuning the substrate morphology and the choice of the material. The edge-terminated MoS_2 film prepared on rough, lapped glassy carbon substrate exhibits a Tafel slope of 86 mV/dec (Supporting Information, Figure S7), whereas edge-terminated MoS_2 film on Mo foil shows a Tafel slope of 75 mV/dec (Supporting Information, Figure S8). The improvements suggest viable avenues to optimize the overall kinect current density of edge-terminated MoS_2 and $MoSe_2$ catalysts.

Stability is another important aspect for electrocatalysts. It is a practical concern for edge-terminated, metastable MoS_2 and $MoSe_2$ films studied here. The long-term stability is assessed by taking continuous cyclic voltammograms in the cathodic potential window at an accelarated scanning rate of 50 mV/s.[42,50] We set the lower potential limits (about −0.4 V for MoS_2 and −0.45 V for $MoSe_2$) to drive a very large cathodic current density of 8 mA/cm^2. The polarization curves before and after cycling are recorded under quasi-equilibrium conditions with a slower scan rate of 2 mV/s. Polarization curves after the 1000th cycle almost overlay the curve of the first cycle with negligible loss of cathodic current, as shown in Figure 6c and d. It confirms that the edge-terminated films of MoS_2 and $MoSe_2$ are stable in acidic electrolyte and remain intact through repeated cycling. Notice that the current cutoff of 8 mA/cm^2 is surface-area-normalized kinetic current, and much higher geometric

dx.doi.org/10.1021/nl400258t | Nano Lett. XXXX, XXX, XXX−XXX

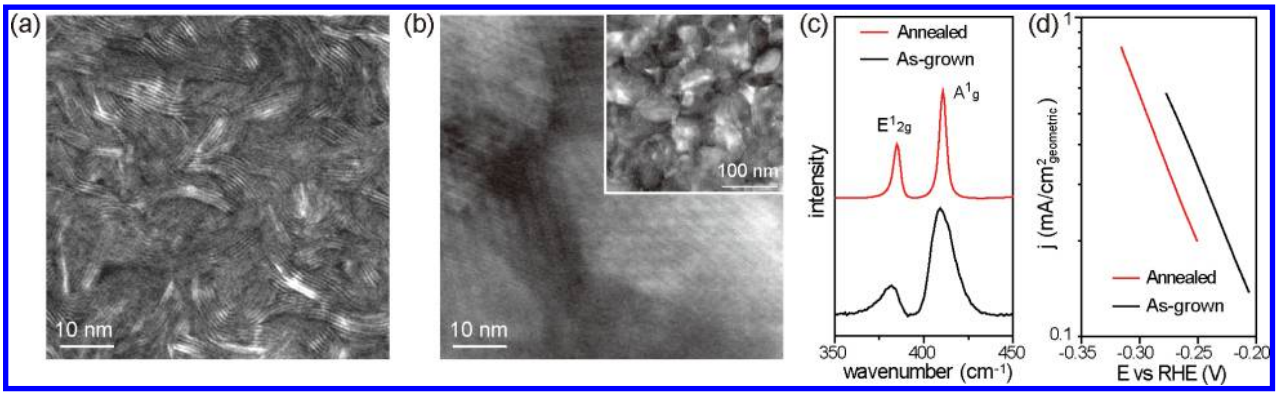

Figure 7. The effect of edges on HER activity studied by thermal annealing of the as-grown films. (a) STEM image of a MoS_2 film, annealed at 550 °C for 2 h, retaining edge-terminated surface. (b) STEM image of a MoS_2 film, annealed at 800 °C for 8 h, with multiple moiré fringes due to the formation of randomly oriented particles. Low-magnification STEM image (inset) reveals the film is composed of plate-like particles on the order of tens of nanometers. (c) Raman spectra from the as-grown and 800 °C-annealed MoS_2 films show E^1_{2g} mode with increased intensity, as well as reduced peak widths and higher crystal quality upon annealing. (d) Tafel plot of the corresponding electrochemical measurements.

kinetic current can potentially be achieved if the films are grown on high surface area substrates.

As the edge-terminated films are a kinetically synthesized product, we attempted to reduce the number of edge sites on the films by annealing, to correlate the edge site density to the catalytic activity. Figure 7a and b present dark field scanning transmission electron microscopy (STEM) images of edge-terminated MoS_2 films annealed at 550 °C for 2h and at 800 °C for 8h, respectively. Annealing at the synthesis temperature of 550 °C does not affect the texture of the film. To reduce the high-energy edge surface, multiple grains should rotate and migrate simultaneously, which imposes a large energy barrier to overcome. Accordingly, our edge-terminated films represent a metastable form of molybdenum chalcogenides. After annealing at 800 °C for an extended period, the film converts into particulate morphology with randomly oriented platelet-like nanoparticles with dimension of tens of nanometers. The growth of these nanoparticles reduces the number of edge sites, which is driven by the tendency to decrease the overall surface energy. In Figure 7c, the relative intensities of Raman modes from 800 °C annealed film lie between the terrace-terminated and edge-terminated films, since the preferential orientation of the layers is lost. The annealed MoS_2 film also exhibits improved crystalline quality, evidenced by the reduction of peak widths in the Raman spectrum. Corresponding electrochemical measurements in Figure 7d indeed show decreased HER activity for the 800 °C annealed film, with much lower exchange current density than as-grown samples. This confirms that the number of edge sites is critical for catalytic activity, whereas the crystalline quality is less important.

The chalcogenide films with high-density edge sites represents a novel metastable structure of layered materials. The unique structure paves the way to use the edges of layered materials more effectively. In particular, the edge-terminated layered chalcogenide films may have broad applications in many important catalytic reactions, including hydrodesulfurization for the petroleum industry,[35] oxygen reduction reactions for fuel cells,[39] and HER studied here.

Methods. *Synthesis and Preparation.* Edge-terminated MoS_2 and $MoSe_2$ films are grown inside a single-zone, 12-in. horizontal tube furnace (Lindberg/Blue M) equipped with a 1-in.-diameter quartz tube. The synthesis setup is illustrated in Figure 2a. The substrates are coated with 5-nm-thick Mo film as a precursor by e-beam evaporation at a low deposition rate of ~0.1 Å/s. Substrates are placed at the hot center of the tube furnace. Sulfur/selenium powder (from Sigma Aldrich) is placed at the upstream side of the furnace at carefully adjusted locations to set the temperature. The tube is pumped to a base pressure of 100 mTorr and flushed with Ar gas to remove residue oxygen. Subsequently, the heating center of the furnace is quickly raised to reaction temperature of 550 °C in 20 min, and the sulfur/selenium precursor is kept at ~220 °C and ~300 °C respectively, well above their melting temperatures. The furnace is held at reaction temperature for 10 min, followed by natural cool-down, during which Ar gas is kept flowing at a rate of 100 s.c.c.m. to transport sulfur/selenium to the substrate. After the reaction, the mass loading is ~8.5 μg/cm^2 for MoS_2 and ~13.5 μg/cm^2 for $MoSe_2$.

Thermal annealing of MoS_2 films are performed in the same setup. During the process, sulfur vapor is supplied in the furnace, to prevent the gradual depletion of sulfur in the film.

MoS_2 single crystal is obtained from SPI Supplies to establish a reference Raman spectrum of the terrace-terminated surface. A fresh terrace-terminated surface is created by cleaving the crystal using Scotch tape.

Characterizations. Characterizations were carried out using TEM (FEI Tecnai G2 F20 X-Twin microscope at 200 keV and aberration-corrected FEI 80-300 environmental Titan (S)TEM microscope at 300 keV), Raman spectroscopy (WITEC Raman spectrometer), X-ray photoelectron spectroscopy (XPS, SSI S-Probe XPS spectrometer with Al(Ka) source), atomic force microcopy (AFM, Park Systems XE-70), and scanning electron microscopy (SEM, FEI Nova NanoSEM 450). Films for TEM characterization are prepared on an oxidized silicon substrate (300 nm SiO_2/Si), followed by a lift-off process to transfer the films onto carbon membranes supported on nickel TEM grids by etching away the sacrificial SiO_2 layer with dilute HF solution. For electron tomography, the sample was tilted to ±64° while taking aberration-corrected TEM images at 1° tilt increments. Gold particles were used to decorate the sample as fiducial markers for postalignment of the tilt series. A weighted back-projection was used to reconstruct the three-dimensional data. Volume-rendering in Amira was used to visualize the reconstructed data. In Figure 1d, the top surface of the reconstruction is replaced with a cross-section of the tomogram to enhance the contrast for clearly visualizing individual layers. Supplementary Movies S11 and S12 show the original reconstructed tomogram of MoS_2 film in different perspectives.

dx.doi.org/10.1021/nl400258t | *Nano Lett.* XXXX, XXX, XXX−XXX

Electrochemical Studies. $MoS_2/MoSe_2$ films are grown on mirror polished glassy carbon (from HTW Hochtemperatur-Werkstoffe GmbH) to measure HER activities. Electrochemically inert, hydrophobic wax (Apiezon wax W-W100) is used to define the 1 cm^2 electrode area. A metal alligator clip is used to connect the working electrode with an external circuit. The measurements are performed in 0.5 M H_2SO_4 solution (deaerated by N_2) using a three electrode setup, with a K_2SO_4 saturated $Hg/HgSO_4$ reference electrode (from AMEL instruments), a graphite rod (99.999%, from Sigma Aldrich) counter electrode, and the glassy carbon working electrode. The reference electrode is calibrated in H_2 saturated electrolyte with respect to an *in situ* reverse hydrogen electrode (RHE), by using two platinum wires as working and counter electrodes, which yields the relation $E(\mathrm{RHE}) = E(\mathrm{Hg/HgSO_4}) + 0.735$ V. The saturation condition is confirmed by minimizing the potential difference between the working and counter electrodes to less than a few mV. Linear sweep voltammetry (scan rate 2 mV/s) and AC impedance spectroscopy (at zero overpotential) are recorded by a Biologic VSP potentiostat. For a Tafel plot, the linear portion at low overpotential, corresponding to cathodic current density of less than 1 mV/cm^2, is fit to the Tafel equation. Within the low overpotential range, the fit is not affected by the evolution of hydrogen bubbles or other kinetic effects. All data have been corrected for a small ohmic drop (<4 Ω) based on impedance spectroscopy.

■ ASSOCIATED CONTENT

Supporting Information

Additional details on sample preparations, chracterizations, electrochemical measurements, and analyses. This material is available free of charge via the Internet at http://pubs.acs.org.

■ AUTHOR INFORMATION

Corresponding Author

*E-mail: yicui@stanford.edu.

Notes

The authors declare no competing financial interest.

■ ACKNOWLEDGMENTS

We acknowledge support by the Department of Energy, Office of Basic Energy Sciences, Materials Sciences and Engineering Division, under contract DE-AC02-76-SFO0515. We thank Peter A. Ercius at National Center for Electron Microscopy, Lawrence Berkeley National Laboratory for his tomography reconstruction scripts. Author contributions are as follows: D.K. and Y.C. conceived the experiments. D.K. and H.W. synthesized and prepared the materials. J.J.C. carried out the TEM characterization and electron tomography reconstruction. D.K., H.W., J.J.C., K.J.K., and J. Y. performed additional characterizations. M.P., D.K., and H.W. performed electrochemical measurements and analyses. All authors contributed to scientific planning and discussions.

■ REFERENCES

(1) Novoselov, K. S.; Geim, A. K.; Morozov, S. V.; Jiang, D.; Zhang, Y.; Dubonos, S. V.; Grigorieva, I. V.; Firsov, A. A. *Science* **2004**, *306* (5696), 666−669.

(2) Novoselov, K. S.; Jiang, D.; Schedin, F.; Booth, T. J.; Khotkevich, V. V.; Morozov, S. V.; Geim, A. K. *Proc. Natl. Acad. Sci. U.S.A.* **2005**, *102* (30), 10451−10453.

(3) Mak, K. F.; Lee, C.; Hone, J.; Shan, J.; Heinz, T. F. *Phys. Rev. Lett.* **2010**, *105* (13), 136805.

(4) Divigalpitiya, W. M. R.; Frindt, R. F.; Morrison, S. R. *Science* **1989**, *246* (4928), 369−371.

(5) Ding, Z.; Viculis, L.; Nakawatase, J.; Kaner, R. B. *Adv. Mater.* **2001**, *13* (11), 797−800.

(6) Hernandez, Y.; Nicolosi, V.; Lotya, M.; Blighe, F. M.; Sun, Z.; De, S.; McGovern, I. T.; Holland, B.; Byrne, M.; Gun'ko, Y. K.; Boland, J. J.; Niraj, P.; Duesberg, G.; Krishnamurthy, S.; Goodhue, R.; Hutchison, J.; Scardaci, V.; Ferrari, A. C.; Coleman, J. N. *Nat. Nanotechnol.* **2008**, *3* (9), 563−568.

(7) Coleman, J. N.; Lotya, M.; O'Neill, A.; Bergin, S. D.; King, P. J.; Khan, U.; Young, K.; Gaucher, A.; De, S.; Smith, R. J.; Shvets, I. V.; Arora, S. K.; Stanton, G.; Kim, H.-Y.; Lee, K.; Kim, G. T.; Duesberg, G. S.; Hallam, T.; Boland, J. J.; Wang, J. J.; Donegan, J. F.; Grunlan, J. C.; Moriarty, G.; Shmeliov, A.; Nicholls, R. J.; Perkins, J. M.; Grieveson, E. M.; Theuwissen, K.; McComb, D. W.; Nellist, P. D.; Nicolosi, V. *Science* **2011**, *331* (6017), 568−571.

(8) Zeng, Z.; Yin, Z.; Huang, X.; Li, H.; He, Q.; Lu, G.; Boey, F.; Zhang, H. *Angew. Chem., Int. Ed.* **2011**, *50* (47), 11093−11097.

(9) Dines, M. B. *Mater. Res. Bull.* **1975**, *10* (4), 287−291.

(10) Kim, F.; Cote, L. J.; Huang, J. *Adv. Mater.* **2010**, *22* (17), 1954−1958.

(11) Eda, G.; Yamaguchi, H.; Voiry, D.; Fujita, T.; Chen, M.; Chhowalla, M. *Nano Lett.* **2011**, *11* (12), 5111−5116.

(12) Li, X.; Cai, W.; An, J.; Kim, S.; Nah, J.; Yang, D.; Piner, R.; Velamakanni, A.; Jung, I.; Tutuc, E.; Banerjee, S. K.; Colombo, L.; Ruoff, R. S. *Science* **2009**, *324* (5932), 1312−1314.

(13) Reina, A.; Jia, X.; Ho, J.; Nezich, D.; Son, H.; Bulovic, V.; Dresselhaus, M. S.; Kong, J. *Nano Lett.* **2008**, *9* (1), 30−35.

(14) Hass, J.; Heer, W. A. d.; Conrad, E. H. *J. Phys.: Condens. Matter* **2008**, *20* (32), 323202.

(15) Venkatasubramanian, R.; Siivola, E.; Colpitts, T.; O'Quinn, B. *Nature* **2001**, *413* (6856), 597−602.

(16) Li, Y.-Y.; Wang, G.; Zhu, X.-G.; Liu, M.-H.; Ye, C.; Chen, X.; Wang, Y.-Y.; He, K.; Wang, L.-L.; Ma, X.-C.; Zhang, H.-J.; Dai, X.; Fang, Z.; Xie, X.-C.; Liu, Y.; Qi, X.-L.; Jia, J.-F.; Zhang, S.-C.; Xue, Q.-K. *Adv. Mater.* **2010**, *22* (36), 4002−4007.

(17) Lee, Y.-H.; Zhang, X.-Q.; Zhang, W.; Chang, M.-T.; Lin, C.-T.; Chang, K.-D.; Yu, Y.-C.; Wang, J. T.-W.; Chang, C.-S.; Li, L.-J.; Lin, T.-W. *Adv. Mater.* **2012**, *24* (17), 2320−2325.

(18) Zhan, Y.; Liu, Z.; Najmaei, S.; Ajayan, P. M.; Lou, J. *Small* **2012**, *8* (7), 966−971.

(19) Liu, K.-K.; Zhang, W.; Lee, Y.-H.; Lin, Y.-C.; Chang, M.-T.; Su, C.-Y.; Chang, C.-S.; Li, H.; Shi, Y.; Zhang, H.; Lai, C.-S.; Li, L.-J. *Nano Lett.* **2012**, *12* (3), 1538−1544.

(20) Shi, Y.; Zhou, W.; Lu, A.-Y.; Fang, W.; Lee, Y.-H.; Hsu, A. L.; Kim, S. M.; Kim, K. K.; Yang, H. Y.; Li, L.-J.; Idrobo, J.-C.; Kong, J. *Nano Lett.* **2012**, *12* (6), 2784−2791.

(21) Peng, H.; Meister, S.; Chan, C. K.; Zhang, X. F.; Cui, Y. *Nano Lett.* **2006**, *7* (1), 199−203.

(22) Kong, D.; Dang, W.; Cha, J. J.; Li, H.; Meister, S.; Peng, H.; Liu, Z.; Cui, Y. *Nano Lett.* **2010**, *10* (6), 2245−2250.

(23) Kong, D.; Randel, J. C.; Peng, H.; Cha, J. J.; Meister, S.; Lai, K.; Chen, Y.; Shen, Z.-X.; Manoharan, H. C.; Cui, Y. *Nano Lett.* **2009**, *10* (1), 329−333.

(24) Tenne, R.; Margulis, L.; Genut, M.; Hodes, G. *Nature* **1992**, *360* (6403), 444−446.

(25) Feldman, Y.; Wasserman, E.; Srolovitz, D. J.; Tenne, R. *Science* **1995**, *267* (5195), 222−225.

(26) Tenne, R. *Nat. Nanotechnol.* **2006**, *1* (2), 103−111.

(27) Castro Neto, A. H.; Guinea, F.; Peres, N. M. R.; Novoselov, K. S.; Geim, A. K. *Rev. Mod. Phys.* **2009**, *81* (1), 109−162.

(28) Kuc, A.; Zibouche, N.; Heine, T. *Phys. Rev. B* **2011**, *83* (24), 245213.

(29) Liu, Y.-H.; Porter, S. H.; Goldberger, J. E. *J. Am. Chem. Soc.* **2012**, *134* (11), 5044−5047.

(30) Radisavljevic, B.; Radenovic, A.; Brivio, J.; Giacometti, V.; Kis, A. *Nat. Nanotechnol.* **2011**, *6* (3), 147−150.

(31) Fang, H.; Chuang, S.; Chang, T. C.; Takei, K.; Takahashi, T.; Javey, A. *Nano Lett.* **2012**, *12* (7), 3788−3792.

(32) Wang, Q. H.; Kalantar-Zadeh, K.; Kis, A.; Coleman, J. N.; Strano, M. S. *Nat. Nanotechnol.* **2012**, *7* (11), 699−712.
(33) Chhowalla, M.; Amaratunga, G. A. J. *Nature* **2000**, *407* (6801), 164−167.
(34) Wang, X.; Li, X.; Zhang, L.; Yoon, Y.; Weber, P. K.; Wang, H.; Guo, J.; Dai, H. *Science* **2009**, *324* (5928), 768−771.
(35) Prins, R.; Debeer, V. H. J.; Somorjai, G. A. *Catal. Rev.—Sci. Eng.* **1989**, *31* (1−2), 1−41.
(36) Salmeron, M.; Somorjai, G. A.; Wold, A.; Chianelli, R.; Liang, K. S. *Chem. Phys. Lett.* **1982**, *90* (2), 105−107.
(37) Hinnemann, B.; Moses, P. G.; Bonde, J.; Jørgensen, K. P.; Nielsen, J. H.; Horch, S.; Chorkendorff, I.; Nørskov, J. K. *J. Am. Chem. Soc.* **2005**, *127* (15), 5308−5309.
(38) Jaramillo, T. F.; Jørgensen, K. P.; Bonde, J.; Nielsen, J. H.; Horch, S.; Chorkendorff, I. *Science* **2007**, *317* (5834), 100−102.
(39) Ahmed, S. M.; Gerischer, H. *Electrochim. Acta* **1979**, *24* (6), 705−711.
(40) Zhu, Q.; Wegener, S. L.; Xie, C.; Uche, O.; Neurock, M.; Marks, T. J. *Nat. Chem.* **2012**, advance online publication.
(41) Kibsgaard, J.; Chen, Z.; Reinecke, B. N.; Jaramillo, T. F. *Nat. Mater.* **2012**, *11* (11), 963−969.
(42) Li, Y.; Wang, H.; Xie, L.; Liang, Y.; Hong, G.; Dai, H. *J. Am. Chem. Soc.* **2011**, *133* (19), 7296−7299.
(43) Nath, M.; Rao, C. N. R. *Chem. Commun.* **2001**, *0* (21), 2236−2237.
(44) Verble, J. L.; Wietling, T. J.; Reed, P. R. *Solid State Commun.* **1972**, *11* (8), 941−944.
(45) Midgley, P. A.; Dunin-Borkowski, R. E. *Nat. Mater.* **2009**, *8* (4), 271−280.
(46) Scott, M. C.; Chen, C.-C.; Mecklenburg, M.; Zhu, C.; Xu, R.; Ercius, P.; Dahmen, U.; Regan, B. C.; Miao, J. *Nature* **2012**, *483* (7390), 444−447.
(47) Midgley, P. A.; Weyland, M. *Ultramicroscopy* **2003**, *96* (3−4), 413−431.
(48) Cha, J. J.; Weyland, M.; Briere, J.-F.; Daykov, I. P.; Arias, T. A.; Muller, D. A. *Nano Lett.* **2007**, *7* (12), 3770−3773.
(49) Verble, J. L.; Wieting, T. J. *Phys. Rev. Lett.* **1970**, *25* (6), 362−365.
(50) Chen, Z.; Cummins, D.; Reinecke, B. N.; Clark, E.; Sunkara, M. K.; Jaramillo, T. F. *Nano Lett.* **2011**, *11* (10), 4168−4175.
(51) Jäger-Waldau, A.; Lux-Steiner, M.; Jäger-Waldau, R.; Burkhardt, R.; Bucher, E. *Thin Solid Films* **1990**, *189* (2), 339−345.
(52) Jäger-Waldau, A.; Lux-Steiner, M. C.; Bucher, E.; Scandella, L.; Schumacher, A.; Prins, R. *Appl. Surf. Sci.* **1993**, *65/66* (0), 465−472.
(53) Laursen, A. B.; Kegnaes, S.; Dahl, S.; Chorkendorff, I. *Energy Environ. Sci.* **2012**, *5* (2), 5577−5591.
(54) Merki, D.; Hu, X. *Energy Environ. Sci.* **2011**, *4* (10), 3878−3888.
(55) Evans, B. L.; Young, P. A. *Proc. R. Soc. London, Ser. A* **1965**, *284* (1398), 402−422.
(56) Hu, S. Y.; Liang, C. H.; Tiong, K. K.; Lee, Y. C.; Huang, Y. S. *J. Cryst. Growth* **2005**, *285* (3), 408−414.
(57) Trasatti, S. *J. Electroanal. Chem. Interf. Electrochem.* **1972**, *39* (1), 163−184.
(58) Kochubey, D. I.; Rogov, V. A.; Babenko, V. P. *React. Kinet. Catal. Lett.* **2007**, *90* (1), 167−177.
(59) Merki, D.; Fierro, S.; Vrubel, H.; Hu, X. *Chem. Sci.* **2011**, *2* (7), 1262−1267.
(60) Jaramillo, T. F.; Bonde, J.; Zhang, J.; Ooi, B.-L.; Andersson, K.; Ulstrup, J.; Chorkendorff, I. *J. Phys. Chem. C* **2008**, *112* (45), 17492−17498.
(61) Karunadasa, H. I.; Montalvo, E.; Sun, Y.; Majda, M.; Long, J. R.; Chang, C. J. *Science* **2012**, *335* (6069), 698−702.
(62) Pentland, N.; Bockris, J. O. M.; Sheldon, E. *J. Electrochem. Soc.* **1957**, *104* (3), 182−194.
(63) Conway, B. E.; Tilak, B. V. *Electrochim. Acta* **2002**, *47* (22−23), 3571−3594.
(64) Bonde, J.; Moses, P. G.; Jaramillo, T. F.; Norskov, J. K.; Chorkendorff, I. *Faraday Discuss.* **2009**, *140*, 219−231.

dx.doi.org/10.1021/nl400258t | *Nano Lett.* XXXX, XXX, XXX−XXX